A unicellular walker embodies a finite state machine

Authors: Ben T. Larson[1], Jack Garbus[2], Jordan B. Pollack[2], and Wallace F. Marshall[1]

[1] Department of Biochemistry and Biophysics, University of California, San Francisco, California, USA

[2] Computer Science Department, Brandeis University, Waltham, Massachusetts, USA

Cells are complex biochemical systems whose behavior emerges from interactions among myriad molecular components. The idea that cells execute computational processes is often invoked as a general framework for understanding cellular complexity. However, the manner in which cells might embody computational processes in a way that the powerful theories of computation, such as finite state machine models, could be productively applied, remains to be seen. Here we demonstrate finite state machine-like processing embodied in cells, using the walking behavior of *Euplotes eurystomus*, a ciliate that walks across surfaces using fourteen motile appendages called cirri. We found that cellular walking entails a discrete set of gait states. Transitions between these states are highly regulated, with distinct breaking of detailed balance and only a small subset of possible transitions actually observed. The set of observed transitions decomposes into a small group of high-probability unbalanced transitions forming a cycle and a large group of low-probability balanced transitions, thus revealing stereotypy in sequential patterns of state transitions. Taken together these findings implicate a machine-like process. Cirri are connected by microtubule bundles, and we find an association between the involvement of cirri in different state transitions and the pattern of attachment to the microtubule bundle system, suggesting a mechanical basis for the regularity of state transitions. We propose a model where the actively controlled, unbalanced transitions establish strain in certain cirri, the release of which from the substrate causes the cell to advance forward along a linear

trajectory. This demonstration of a finite state machine embodied in a living cell opens up new links between theoretical computer science and cell biology and may provide a general framework for understanding and predicting cell behavior at a super-molecular level.

Introduction

Cells are complex physical systems controlled by networks of signaling molecules. Single cells can display remarkably sophisticated, seemingly animal-like behaviors [1–3], orchestrating active processes far from thermodynamic equilibrium in order to carry out proper biological functions [4,5]. Indeed, single cells can make decisions by sensing and responding to diverse cues and signals [6], execute coordinated movements [7,8] and directed motility [9–12], and even solve mazes [13,14] and possibly learn [15–18]. Such behaviors in animals arise from neural activity and have been studied extensively, but we know comparatively little about the mechanisms of cellular behavior [19,20]. In individual cells, behaviors emerge directly through the joint action of chemical reactions [21], cellular architecture [3], physical mechanisms and constraints within the cell [22,23] and interactions of the cell with its local environment [24]. The links between information processing, decision-making, and their physical manifestation as cell state transitions suggest that cellular behavior might be understood as an embodied computation [25,26]. The theory of computation has often been invoked as a general framework for understanding cellular dynamics [25,27–32], with environmental sensing by bacteria being a particularly deeply studied example [32–34], and has been used to engineer programmable cell states [35], but the manner and extent to which cells might embody functional, computational processes as well as the extent to which a computational perspective on cellular behavior might prove productive remains to be seen.

Among the microbial eukaryotes (protists), ciliates display striking examples of unicellular behavior including hunting [3], sensorimotor navigation [10], and predator avoidance [36]. Spirotrichous ciliates of the genus *Euplotes* are notable for their complex locomotion [37–39], using bundles of specialized cilia called cirri to walk across surfaces [37,38] (Fig. 1a, Movies S1 and S2). Depending on the species, cells generally have 14 to 15 ventral cirri arranged in a highly stereotyped pattern used for walking locomotion [40]. *Euplotes* live in aquatic environments, and in addition to walking, their cirri can be used for swimming and rapid escape responses [41] (Movie S2). Oral membranelles (Fig. 1b) generate feeding currents to capture bacteria and small protistan prey and are also used for swimming. Early 20th century protistologists were so impressed by the apparent coordination of cirri that they proposed the existence of a rudimentary nervous system, the neuromotor apparatus, to account for their observations [39]. This theory was motivated in part by the presence of intracellular fibers connecting various cirri (Fig. 1C), now known to be to be tubulin-based structures [42,43]. Although the walking movements of *Euplotes* are superficially similar to those of animals such as insects, the low Reynolds environment of aquatic microorganisms, where viscous forces dominate over inertial forces, imposes significant physical constraints on all movements that do not impinge on the movements of larger terrestrial animals [44].

How can a single cell coordinate a gait without a nervous system? Coordination, to the extent that it exists in the gait of *Euplotes*, would require some kind of dynamical coupling among cirri or between cirri and some shared external influence. Recently, analytical techniques from statistical physics have been used to characterize, understand, and predict mesoscale dynamics in biological systems, including cellular behavior [4,5,45,46]. These approaches rely on coarse-graining the complexity of biological dynamics into states and analyzing the nature of

transitions between states. For example, a state representation allows us to ask whether forward and reverse transitions between pairs of states are equal, a condition known as detailed balance [4,47]. Systems that violate detailed balance operate in a non-equilibrium mode and can produce directed cycles in state space [4,48]. Broken detailed balance has been observed in the motility dynamics of cultured mammalian cells as well as the motility dynamics of a freely behaving flagellate protist [5,45] and implies that non-equilibrium models are most applicable to such systems [46].

When information processing drives patterns of state transitions, such a system can be viewed in terms of automata theory, a fundamental level in the theory of computation [49–51].Automata theory can be used to address problems of decision-making and control in complex systems by providing predictive understanding independently of the underlying details of how a given process is implemented [50]. Inspired by work considering cellular behavior in the context of the theory of computation [25], we hypothesized that walking cells might be governed by finite state automata with directed, processive movement arising from reproducible patterns of state transitions.

The consistent structure of *Euplotes*, its mode of motility, and its ease of observation makes these cells an ideal biological test-bed in which to apply theories of non-equilibrium statistical mechanics and embodied computation, both of which rely on describing a system in terms of discrete state transitions. Here, we use time-lapse microscopy and quantitative analyses to show that *Euplotes eurystomus* walks with a cyclic stochastic gait displaying broken detailed balance and exhibiting elements of stereotypy and variability, consistent with a finite state automaton representation. The observed dynamics are reminiscent of behavioral regulation in some cells and animals [5,52] but contrast with many well-characterized examples of cellular

motility [7,9,10,12,53–56]. Our results provide a clear demonstration of machine-like processes governing cellular state transitions and serve as a framework for investigating the principles of behavioral control and non-equilibrium dynamics in single cells.

Results

Walking dynamics can be described in a reduced state space

In order to ask whether cell behavior is governed by a finite state machine, we analyzed the walking behavior of *Euplotes eurystomus* cells, [41], focusing on the simplest case of uninterrupted, linear walking trajectories (Fig. 2a, b, Movie S1). Cells were placed onto coverslips on which free, spontaneous walking behavior was observed by microscopy. A focal plane at the cirrus-coverslip interface was chosen in order to clearly observe cirral dynamics (Fig. 2a). The relative spatial positioning of cirri is highly stereotyped from cell to cell, allowing us to give each of the 14 cirri an alphabetic label from a-n (Figure 2c). In each video frame (33 frames/s), the walking state of the cell was encoded as a 14-bit binary vector, with each bit corresponding to a cirrus and receiving a value of "0" if the cirrus was in contact with the coverslip and stationary and a "1" if the cirrus was in motion (instances of stationary cirri held above the coverslip for a sustained period of time were not observed). The trajectories of 13 cells were manually tracked and annotated for a total of 2343 time points. This quantitative analysis revealed stepping-like cirral dynamics in that cirri tend to undergo rapid movements followed by longer periods of quiescence (Fig. 2d). Cirral dynamics appeared to lack any obvious patterns such as periodicity or repeating sequences of states (e.g. Fig. 2d), implying that the state sequences are either stochastic, or generated by complex deterministic processes. This lack of periodicity or fixed phase relationships between appendage movements is different from the gaits

117 of most animals or those reported for various flagellates [57–59]. Autocorrelation analysis confirmed
118 the observed lack of clear periodicity (Fig. S1).

119 Despite the apparent complexity of cirral dynamics, we suspected that discernable
120 structure might exist, which would allow us to obtain a reduced state space that accurately
121 described the dynamics as has proved successful in behavioral analysis of diverse living systems
122 [45,46,60–63]. We performed dimensionality reduction using non-negative matrix factorization
123 (NMF), and cross-validation by imputation [64,65] (see Methods and Fig. S2 for more details)
124 revealed the cirral states to be well-described in three dimensions (Fig. 2e-g). The components of
125 the NMF analysis correspond to distinct groups of cirri, and these groups constitute spatially
126 distinct partitions of cirri with respect to their positions on the cell body (Fig. 3h). The
127 dimensionality reduction of the gait state space arises at least in part from shared pairwise mutual
128 information between groups of cirri (Fig. 3i).

129 We next used the density-based spatial clustering of applications with noise (DBSCAN)
130 algorithm [66] to group our data into clusters in an unbiased fashion, with members of a given
131 cluster sharing similar patterns of cirral activity. Visual inspection in conjunction with silhouette
132 coefficient [67] (a metric of cluster cohesion and separation) analysis revealed that 32 clusters
133 accurately captured the visible structure in the reduced state space without overfitting (Fig. 2e-g,
134 see Methods and Fig. S3 for more details)[*]. These reduced gait states correspond to distinct
135 patterns of cirral activity (Fig. 2j). Taken together, our results reveal stereotypy in the
136 spatiotemporal patterns of cirral activity. The discrete, reduced state space, or set of gait states,

[*] The problem of determining the true number of clusters is an unresolved problem [90]. We have followed standard methods to determine cluster number but have found that our key results do not depend sensitively on the precise number of clusters identified (see SI and Fig. S7).

137 demonstrates that cells make use of a subset of the possible patterns of appendage movement
138 during walking locomotion.

139 ***Euplotes walks with a cyclic stochastic gait***

140 In order to relate the gait states identified in our cluster analysis, we asked how changes
141 in the number of active cirri may relate to cell movement. Naively, one might expect that the
142 force associated with locomotion is roughly proportional to the number of moving appendages [68].
143 Alternatively, we velocity might inversely correlate with the net change in cirral activity, which
144 would be expected if stationary cirri were generating a pushing traction force as in crawling or
145 climbing animals [58,69] or if cirri execute a power stroke just before coming to rest as has been
146 suggested by Erra et al. [38]. At low Reynolds number, velocity should be proportional to the
147 difference between the net force generated by the cell and the opposing drag [44]. Examining cell
148 velocity versus the net change in cirral activity, however, showed that neither of these
149 expectations were in fact the case (Fig. 3a). Cell velocity was only weakly correlated with
150 number of active cirri (R^2=0.03), and instead, small to moderate positive and negative changes in
151 the number of active cirri corresponded to the largest cell velocities (Fig. 3a). We reasoned that
152 transitions between gait states must be important to driving the forward progression of walking
153 cells, and so sought to determine whether this active coordination might manifest in the observed
154 gait dynamics.

155 Analysis of the 1423 pairwise transitions in our dataset yielded the transition matrix
156 displayed in Fig. 3b (see Methods for more details). The presence of strongly unbalanced
157 transitions such as from gait state 3 to 17 versus 17 to 3 suggested broken detailed balance, and
158 indeed, a number of forward and reverse transitions were found to be significantly unbalanced by
159 the binomial test (see Methods). Entropy production rate has been used to quantify the degree of

160 broken detailed balance, or, similarly, the distance from equilibrium where the entropy
161 production rate will be zero [5]. Following the procedure detailed in [5], we obtain a lower bound
162 estimate for an entropy production rate of 0.4, similar to the value reported for strongly non-
163 equilibrium gait transitions observed in a flagellate [5]. Walking *Euplotes* cells, therefore, have a
164 strongly non-equilibrium gait despite lack of periodicity.

165 Only 322 of the 1024 possible types of transitions were observed to occur at least once,
166 and within this restricted set, only 173 occurred more than once (Fig. 3c). Also, we found that
167 relatively few transitions corresponded to substantial cellular movement (Fig. 3c). Crucially, the
168 presence of broken detailed balance revealed the existence of directed cycles of cirral activity
169 during locomotion. To get a better understanding of the nature of these cycles, we grouped
170 transitions into two categories: balanced transitions, which satisfy detailed balance, and
171 unbalanced transitions, which do not (see Methods for details). This partitioning allowed us to
172 separately investigate unbalanced, non-equilibrium-like and balanced, equilibrium-like
173 transitions (Fig. 3d, e). Significantly unbalanced transitions ($p<0.05$ by binomial test) are among
174 the most frequent transitions, but only involve a small number of states (Fig. 3d). Of the 32 gait
175 states, we found that only states 2, 3, 4, 7, 17, and 27 were associated with unbalanced
176 transitions. We noted the presence of one complete cycle with unbalanced transitions following
177 2→3→17→2. We had expected that unbalanced transitions might be associated with a "power
178 stroke" in the sense of occurring simultaneously with cell movement, but in fact high cellular
179 velocities tended to be associated with balanced transitions (Fig. 3d, e). Additionally, we found
180 that, with the exception of transitions between states 1 and 2, transitions occurring at the highest
181 frequencies were unbalanced (Fig. 3d).

182 Notably, the most frequent balanced transitions were associated with transitions into and
183 out of gait state 1, a unique "rest state" which involves no cirral movement (Fig. 3c, d).
184 Furthermore, we found by computing the autocorrelation function for a binarized sequence of
185 each state that gait state 1 has the most predictable dynamics in terms of significant positive
186 autocorrelation in contrast to the lack of significant autocorrelation seen for other states (see Fig.
187 S4). Although transitions between states 1 and 2 are balanced, the most frequent transitions out
188 of state 2 are strongly biased toward transitions into state 3, from which other strongly biased
189 transitions also frequently occur, including the cycle of biased transitions mentioned in the
190 preceding paragraph. The presence of high frequency unbalanced transitions does not preclude
191 the existence of highly variable trajectories through state space. The picture of walking
192 trajectories that emerges is of stochastic excursions from gait state 1 into a stochastic cycle
193 involving a mix of balanced and unbalanced transitions, with the majority of cell movement
194 occurring during infrequent, equilibrium-like transitions. Biased transitions, occurring at
195 relatively high frequency from a subset of states, introduce temporal irreversibility to the gait of
196 *Euplotes* due to their strongly non-equilibrium character.
197 Finally, we checked whether gait state transition dynamics had the Markov property,
198 which entails that transition probabilities are determined completely by the present state, and that
199 previous dynamics contribute no additional predictive information [70,71]. Lack of past dependence
200 has led to Markov processes often being referred to as "memoryless" [72]. When we compared the
201 gait transition matrix (Fig. 3b) with a computed transition matrix over two timesteps, we
202 observed these matrices to be different from one another, which is inconsistent with the Markov
203 property (see Fig. S5). Finally, we applied a Billingsley test, a chi-squared measure for
204 Markovness [73], which revealed that the null hypothesis that the process was Markov could be

205 rejected (p=0.005). These analyses showed that *Euplotes* retains some "memory" of the prior
206 sequence of cirral movements during locomotion.

207 Taken together, our analysis revealed a mixture of unbalanced transitions arranged in
208 cycles and balanced transitions arranged as networks, for which we propose to apply the term
209 "cyclic stochastic gait". The cyclic stochastic gait of *Euplotes eurystomus* incorporates elements
210 of both stereotypy and variability in gait dynamics. Forward progress of the cell is not produced
211 merely by a physical ratchetting process driven by unpatterned fluctuations in cirral activity, nor
212 is it produced by a highly regular, deterministic process like a clock. It has been argued that
213 significant computation arises in physical systems exhibiting such a mix of stereotypy and
214 variability [49,74–76] in the sense that the time-evolution of the system is most compactly described
215 by the result of a computation involving state transitions, memory, and decision rules, rather than
216 by a periodic oscillation or a random coin flip.

217 While our analysis revealed a computational underpinning of gait, we sought to better
218 understand the functional organization of the dynamical patterns driving processive motion of
219 the cell. To do so, we first focused on the highest transition probabilities emanating from each
220 state. Transition probabilities were estimated as N_{ij}/N_i where N_{ij} is the number of transitions from
221 state i to state j, and N_i is the total number of transitions from state i. This allowed us to prune
222 away rare transitions in order to reveal the dominant structure of gait state transitions. Figure 3g
223 displays the pruned transition matrix as a heatmap. We found that relatively few states were the
224 recipients of the majority of high probability transitions, and many states received none. To more
225 clearly visualize the structure of transitions, we grouped together all gait states receiving no more
226 than one unique high probability transition with the idea being that state transitions into this
227 group show little bias in terms of source state, and within the group, transitions between states

228 exhibit low probability, time unbiased, equilibrium-like fluctuations. the majority of cell
229 movement was associated with transitions between states within this group. In contrast to the
230 "cloud" of states linked by low-probability, balanced transitions, nearly all of the states receiving
231 high probability transitions were either the three "cycle" states, or else fed cycle states with their
232 highest probability transitions, with the majority feeding gait state 17.

233 Focusing on the structure of transitions in this way allowed us to derive a simplified,
234 functional representation of stereotypy in gait dynamics as depicted in Fig. 3h. Although gait
235 state 1 is not the recipient of any individual high probability transitions, we identified it as the
236 unique "start" state from which cells initiate walking. Beginning with this start state, cells
237 transition with high probability to gait state 2, also one of the highest frequency transitions and
238 the first state in the 2→3→17→2 cycle of unbalanced transitions. From this first cycle state,
239 cells transition to gait state 3, the second cycle state, with highest probability and frequency and
240 then similarly on to gait state 17, the third cycle state. This sequence from the start state through
241 the cycle states corresponds to increasing amounts of cirral activity. Although the highest
242 probability transitions from the third cycle state to any single gait state return to the first and
243 second cycle state with equal probability and return to the first cycle state also being unbalanced,
244 cells in fact transition to the equilibrium "cloud" of motility-associated states with overall higher
245 probability. Return to the cycle states tend to occur through various moderately high probability
246 transitions from the motility state cloud or through intermediate states. In conjunction with this
247 set of transitions, we also noted unbalanced transitions stemming from the cycle states to the
248 motility state as well as intermediate state subsequently feeding the next cycle state.

249 Altogether, the picture that emerges of stereotypical gait dynamics is of biased transitions
250 through cycle states before relatively low probability, unbiased transitions associated with

251 substantial cell movement before returning to the start or cycle states and beginning the sequence
252 again. While this general sequence is repeated during walking, there is variability or apparent
253 stochasticity in the details of gait state transitions with increasingly variable transitions as any
254 given sequence progresses. We propose that the cycle states serve to establish configurations of
255 cirri necessary for cells to later transition to between states from which forward progress of the
256 cell is generated. Many state transitions along any instance of the stereotyped sequence are
257 unbiased, but biased, high probability transitions, presumably resulting from active cellular
258 control, give temporal irreversibility to the sequence.
259
260 ***The fiber system of Euplotes constrains models of gait coordination***
261 What physical machinery could embody this information processing required to generate
262 the stochastic cyclic state transitions seen during *Euplotes*' walking? We reasoned that there
263 must be some form of coupling or communication between cirri or feedback between gait state
264 and cirral dynamics. The role of the system of cytoskeletal fibers associated with cirri as conduits
265 of information between cirri during cellular locomotion, supported by microsurgical
266 experiments, has been a key hypothesized mechanism of gait coordination since the early 1900s
267 [77,78]. We wondered whether the structure of the cytoskeletal fiber system associated with cirri
268 (Fig. 4a) could give some insight into how cirri might be coordinated.
269 We sought to characterize and reconstruct in 3D the tubulin-based fiber system of
270 *Euplotes* associated with cirri and lying just beneath the cell cortex [39,42,43]. Upon inspection of
271 our confocal reconstructions of SiR-tubulin labeled cells (Fig. 4a, Fig. S6), we noted the
272 presence of two morphologically distinct classes of fibers, one thicker, linear class and the other
273 more filamentous and less linear, consistent with previous observations (Fig. 1c, [39,42,43]).

274 Additionally, we observed a group of thick linear fibers associated with some of the frontal cirri,
275 which to our knowledge has not been previously reported. Fibers emanate from the base of all
276 cirri, appear to intersect one another, and also connect to the cortex of the cell at various points
277 (Fig. 3g). Some cirri were found to be associated with only thick fibers while others have both or
278 only thin fibers. Based on apparent fiber intersections and convergences, we found the fiber
279 system to constitute a continuous network between all cirri, with the fibers associated with the
280 base of each cirrus intersecting the fiber system associated with at least one other cirrus (Fig. 4a,
281 b). Contrary to the long-standing standing hypothesis from the literature [77], the functional
282 modules (groups of co-varying cirri) identified in our dynamical analysis were not exclusively
283 linked by dense fiber intersections [39,43,77] (Fig. 4a, b). In fact, connections between cirri are not
284 generally associated with any statistically significant difference in mutual information (defined
285 in terms of the information that the activation state of one cirrus has concerning the other)
286 compared to unlinked pairs of cirri ($p=0.14$ by Wilcoxon rank sum test, Fig. 4C). However,
287 information flow became apparent when fiber-fiber links are grouped by type (i.e. thick to thick
288 fiber, thick to thin fiber, or thin to thin fiber). We found that pairs of cirri associated with only
289 thick fiber to thick fiber and only thin fiber to thin fiber links have increased mutual information
290 compared to those without links (Fig. S6). Interestingly, we found that cirri nearby one another
291 and connected by fibers to similar regions of the cell cortex shared the most mutual information
292 (Fig. 2i, 3c, 4d, e), suggesting that if the fibers play a role in cirral coordination, coupling may
293 also be mediated by mechanisms at the cirrus and fiber-cortex interface. Cirri d, e, h, i, for
294 example, share very little mutual information with any of the other cirri, and fibers emanating
295 from the base of these cirri contact the cell cortex and other fibers at various unique points. Cirri
296 g and f, on the other hand, which share more mutual information than any other pair, are

297 associated with both thick and thin fibers terminating at similar regions of the cell cortex. Indeed,
298 both distances between pairs of cirri and cross nearest neighbor distance (a measure of similarity
299 between discrete spatial distributions) between paired sets of cirrus-cortex contact points show
300 significant Spearman correlations to mutual information (-0.49, $p<0.001$ and -0.62, $p<0.001$
301 respectively) (Fig. 4d, e). These correlations indicate that mutual information between pairs of
302 cirri tends to increase with proximity and also tends to increase with similarity between fiber-
303 cortex contact locations, so the cirri with the highest mutual information are those that are close
304 together with similar fiber-cortex connections (Fig. 4d-f). Together, these observations strongly
305 support a mechanical coordination mechanism in which microtubule bundles allow groups of
306 cirri to influence successive behavior of other groups of cilia.
307

308 **Discussion**

309 In order to meet the challenge of accounting for the emergence of apparently
310 sophisticated cellular behavior, we conceptualized the cell as a finite state machine.
311 Traditionally, studies of computational processes performed by cells have tended to focused on
312 combinatorial logic, where the output of a computational process depends only on the current
313 input, performed by networks of molecules in bacterial cells [25,32–34]. We have focused on
314 sequential logic, where outputs depend on the system state as well, an equally important aspect
315 of the theory of computation with notable yet less developed representation in studies of cellular
316 and sub-cellular dynamics [16,20,79]. Behavior of eukaryotes has frequently been observed to
317 involve stereotyped transitions between dynamical states, and our results suggest that automata
318 theory, which includes finite state machine models and necessarily involves sequential logic,
319 may be particularly well-suited to studying the behavior of eukaryotic cells. Our approach,

320 relying on dimensionality reduction to identify dynamical states, revealed modularity in cellular
321 dynamics associated with structural modularity of the cell (Fig. 2, 4) in addition to cyclic
322 patterns of sequential dynamical activity (Fig. 3).

323 Walking locomotion in *Euplotes* represents a departure from many of the best studied
324 appendage-based locomotor systems. For example, limbed locomotion in animals tends to
325 proceed by highly stereotyped, determinate patterns of activity [57,58], and many small, aquatic
326 animals exhibit periodic movements of appendages, often cilia, during locomotion [7,59,80]. Many
327 forms of unicellular locomotion involve such dynamics as well including in sperm cells [81],
328 diverse flagellates with various numbers of flagella [59], and ciliates [59,82,83]. Even in cases where
329 cellular locomotion involves fundamentally stochastic dynamics such as in run-and-tumble
330 motility in *E. coli* [12] or analogous behaviors observed in protists [11,84–86], motility can be described
331 by equilibrium processes [5], in contrast to the non-equilibrium character of the gait of *Euplotes*.
332 There are examples, however, of locomotor dynamics in both animals and unicellular organisms
333 that are reminiscent of those we have observed in *Euplotes*. Gait switching in kangaroo rats has
334 been shown to have a stochastic, non-equilibrium character, perhaps to facilitate predator
335 avoidance by being difficult to predict [52]. Most saliently, gait switching in an octoflagellate [5] and
336 motility dynamics in cultured mammalian cells [45] have been shown to exhibit broken detailed
337 balance. We propose that broken detailed balance in the gait of *Euplotes* indicates active
338 coordination of motility processes. Here, broken detailed balance in gait state transitions revealed
339 cyclic activity, characterized by transitions into and out of a resting state with a mixture of
340 stereotypy and variability in the intervening steps, in the gait of a single cell (Fig. 3, 4). To
341 explain how these dynamics give rise to directed walking, we propose a mechanism in which
342 biased, actively controlled cyclic transitions serve to establish strain, effectively storing stress, in

343 certain cirri, and the spontaneous release of these cirri from the substrate, during a series of
344 unbiased gait state transitions, allows the cell to move forward. The cloud of unbiased transitions
345 associated with substantial cellular movement is consistent with the fact that the details of the
346 precise order in which the strained cirri are released does not matter for generating motility.
347 Consistent with this mechanism, inspection of videos revealed that substantial cell movement
348 appears to be correlated with the movement of notably bent inactive cirri. Return to the cycle
349 states then are necessary to establish this process anew by winding up the system for continued
350 cell movement. This mechanism and these patterns of cirral activity are consistent with previous
351 observations of cyclic velocity fluctuations in the trajectories of walking *Euplotes* [37]. We argue
352 that subcellular processes must be involved in actively coordinating cirri in order to accomplish
353 the observed stereotypy in biased sequential activity. Our analysis of the tubulin-based
354 cytoskeletal fiber system is consistent with its role in mechanically mediating communication
355 among cirri and between cirri and cell cortex (Fig. 4). Thus, by combining information
356 processing to properly dictate patterns of cirral activity and the mechanical actions of cirral
357 movement, walking *Euplotes* embodies the sequential computation of a finite state machine.
358 Among the domains of life, eukaryotes uniquely display remarkable complexity and
359 diversity in cellular behavior [87]. Our approach, grounded in finite state-machine analysis, has
360 revealed modularity and stereotypy underlying a complex cellular behavior, implicating a
361 machine-like process. Our results suggest that integrating approaches from theoretical computer
362 science, non-equilibrium statistical physics, and cell biology stands to shed light on the
363 regulation of cellular behavior in eukaryotes more broadly. By revealing principles of cellular
364 behavior, the line of research established here stands to advance our ability to predict and even
365 one day engineer cellular behavior across diverse eukaryotic systems.

366

367 **References**

368 1. Jennings, H. S. *Behavior of the lower organisms. Behavior of the lower organisms.*
369 (Columbia University Press, 1906). doi:10.1037/10817-000

370 2. Reid, C. R. *et al.* Decision-making without a brain: how an amoeboid organism solves the
371 two-armed bandit. *J. R. Soc. Interface* **13**, 20160030 (2016).

372 3. Coyle, S. M., Flaum, E. M., Li, H., Krishnamurthy, D. & Prakash, M. Coupled Active
373 Systems Encode an Emergent Hunting Behavior in the Unicellular Predator Lacrymaria
374 olor. *Curr. Biol.* **29**, 3838-3850.e3 (2019).

375 4. Battle, C. *et al.* Broken detailed balance at mesoscopic scales in active biological systems.
376 *Science* **352**, 604–7 (2016).

377 5. Wan, K. Y. & Goldstein, R. E. Time Irreversibility and Criticality in the Motility of a
378 Flagellate Microorganism. *Phys. Rev. Lett.* **121**, 58103 (2018).

379 6. Woznica, A. *et al.* Bacterial lipids activate, synergize, and inhibit a developmental switch
380 in choanoflagellates. *Proc. Natl. Acad. Sci. U. S. A.* **113**, 7894–7899 (2016).

381 7. Wan, K. Y. Coordination of eukaryotic cilia and flagella. *Essays Biochem.* **62**, 829–838
382 (2018).

383 8. Nomura, M. & Ishida, K. I. Fine-structural Observations on Siliceous Scale Production
384 and Shell Assembly in the Testate Amoeba Paulinella chromatophora. *Protist* **167**, 303–
385 318 (2016).

386 9. Bennett, R. R. & Golestanian, R. A steering mechanism for phototaxis in
387 Chlamydomonas. *J. R. Soc. Interface* **12**, 20141164–20141164 (2015).

388 10. Machemer, H. The swimming cell and its world: Structures and mechanisms of orientation

389 in protists. *Eur. J. Protistol.* **37**, 3–14 (2001).

390 11. Almagor, M., Ron, A. & Bar-Tana, J. Chemotaxis in Tetrahymena thermophila. *Cell*
391 *Motil.* **1**, 261–268 (1981).

392 12. Berg, H. C. & Brown, D. A. Chemotaxis in Escherichia coli analysed by three-
393 dimensional tracking. *Nature* **239**, 500–504 (1972).

394 13. Nakagaki, T., Yamada, H. & Tóth, Á. Maze-solving by an amoeboid organism. *Nature*
395 **407**, 470–470 (2000).

396 14. Tweedy, L. *et al.* Seeing around corners: Cells solve mazes and respond at a distance
397 using attractant breakdown. *Science (80-.).* **369**, (2020).

398 15. Applewhite, P. B. Learning in Protozoa. in *Biochemistry and Physiology of Protozoa* 341–
399 355 (Elsevier, 1979). doi:10.1016/b978-0-12-444601-4.50018-7

400 16. Dexter, J. P., Prabakaran, S. & Gunawardena, J. A Complex Hierarchy of Avoidance
401 Behaviors in a Single-Cell Eukaryote. *Curr. Biol.* **29**, 4323-4329.e2 (2019).

402 17. Jennings, H. S. Studies on reactions to stimuli in unicellular organisms. IX—On the
403 behavior of fixed infusoria (Stentor and Vorticella), with special reference to the
404 modifiability of protozoan reactions. *Am. J. Physiol. Content* **8**, 23–60 (1902).

405 18. Tang, S. K. Y. & Marshall, W. F. Cell learning. *Current Biology* **28**, R1180–R1184
406 (2018).

407 19. Lyon, P. The cognitive cell: Bacterial behavior reconsidered. *Frontiers in Microbiology* **6**,
408 (2015).

409 20. Marshall, W. F. Cellular Cognition: Sequential Logic in a Giant Protist. *Current Biology*
410 **29**, R1303–R1305 (2019).

411 21. Greenfield, D. *et al.* Self-Organization of the Escherichia coli Chemotaxis Network

412 Imaged with Super-Resolution Light Microscopy. *PLoS Biol.* **7**, e1000137 (2009).

413 22. Wan, K. Y. & Goldstein, R. E. Coordinated beating of algal flagella is mediated by basal
414 coupling. *Proc. Natl. Acad. Sci. U. S. A.* **113**, E2784-93 (2016).

415 23. Höfer, T., Sherratt, J. A. & Maini, P. K. Dictyostelium discoideum : cellular self-
416 organization in an excitable biological medium. *Proc. R. Soc. London. Ser. B Biol. Sci.*
417 **259**, 249–257 (1995).

418 24. Kantsler, V., Dunkel, J., Polin, M. & Goldstein, R. E. Ciliary contact interactions
419 dominate surface scattering of swimming eukaryotes. *Proc. Natl. Acad. Sci. U. S. A.* **110**,
420 1187–1192 (2013).

421 25. Bray, D. *Wetware*. (Yale University Press, 2009).

422 26. Pfeifer, R., Lungarella, M. & Iida, F. Self-organization, embodiment, and biologically
423 inspired robotics. *Science* **318**, 1088–1093 (2007).

424 27. Regev, A. & Shapiro, E. Cellular abstractions: Cells as computation. *Nature* **419**, 343–343
425 (2002).

426 28. Mitchell, M. Biological Computation. *Comput. J.* **55**, 852–855 (2012).

427 29. Navlakha, S. & Bar-Joseph, Z. Algorithms in nature: the convergence of systems biology
428 and computational thinking. *Mol. Syst. Biol.* **7**, 546 (2011).

429 30. Savin, T. *et al.* On the growth and form of the gut. *Nature* **476**, 57–62 (2011).

430 31. Mehta, P. & Schwab, D. J. Energetic costs of cellular computation. *Proc. Natl. Acad. Sci.*
431 *U. S. A.* **109**, (2012).

432 32. Berg, H. C. & Purcell, E. M. Physics of chemoreception. *Biophys. J.* **20**, 193–219 (1977).

433 33. Bialek, W. & Setayeshgar, S. Physical limits to biochemical signaling. *Proc. Natl. Acad.*
434 *Sci. U. S. A.* **102**, 10040–5 (2005).

435 34. Mehta, P. & Schwab, D. J. Energetic costs of cellular computation. *Proc. Natl. Acad. Sci.*
436 *U. S. A.* **109**, 17978–17982 (2012).
437 35. Andrews, L. B., Nielsen, A. A. K. & Voigt, C. A. Cellular checkpoint control using
438 programmable sequential logic. *Science (80-.).* **361**, (2018).
439 36. Gilbert, J. J. Jumping behavior in the oligotrich ciliates Strobilidium velox and Halteria
440 grandinella, and its significance as a defense against rotifer predators. *Microb. Ecol.* **27**,
441 189–200 (1994).
442 37. Lueken, W., Ricci, N. & Krüppel, T. Rhythmic spontaneous depolarizations determine a
443 slow-and-fast rhythm in walking of the marine hypotrich Euplotes vannus. *Eur. J.*
444 *Protistol.* **32**, 47–54 (1996).
445 38. Erra, F., Iervasi, A., Ricci, N. & Banchetti, R. Movement of the cirri during the creeping
446 of Euplotes crassus (Ciliata, Hypotrichida). *Can. J. Zool.* **79**, 1353–1362 (2001).
447 39. Taylor, C. V. The neuromotor system of Euplotes. *Exp. Biol. Med.* **16**, 101–103 (1919).
448 40. Syberg-Olsen, M. J. *et al.* Biogeography and character evolution of the ciliate genus
449 Euplotes (Spirotrichea, Euplotia), with description of Euplotes curdsi sp. nov. *PLoS One*
450 **11**, (2016).
451 41. Ricci, N., Giannetti, R. & Miceli, C. The ethogram of Euplotes crassus (ciliata,
452 hypotrichida): I. The wild type. *Eur. J. Protistol.* **23**, 129–140 (1988).
453 42. Li, Y., Shi, L. & Gu, F. Comparison of ciliature microtubule organelles in three
454 hypotrichous ciliate species*. *Chinese J. Oceanol. Limnol.* **28**, 443–450 (2010).
455 43. Fleury, A. Dynamics of the cytoskeleton during morphogenesis in the ciliate Euplotes I.
456 Basal bodies related microtubular system. *Eur. J. Protistol.* **27**, 99–114 (1991).
457 44. Purcell, E. M. Life at low Reynolds number. *Am. J. Phys.* **45**, 3–11 (1977).

458 45. Kimmel, J. C., Chang, A. Y., Brack, A. S. & Marshall, W. F. Inferring cell state by
459 quantitative motility analysis reveals a dynamic state system and broken detailed balance.
460 *PLoS Comput. Biol.* **14**, e1005927 (2018).
461 46. Chang, A. Y. & Marshall, W. F. Dynamics of living cells in a cytomorphological state
462 space. *Proc. Natl. Acad. Sci. U. S. A.* **116**, 21556–21562 (2019).
463 47. Boltzmann, L. Weirere Studien uber das warmegleich-gewich unter gasmolekulen.
464 *Sitzungsberichte der Akad. der Wissenschaften, Vienna, part II* **66**, 275–370 (1872).
465 48. Alberts, B. *et al. Molecular biology of the cell*. (Garland Science, 2002).
466 49. Shalizi, C. R. & Crutchfield, J. P. Computational Mechanics: Pattern and Prediction,
467 Structure and Simplicity. *J. Stat. Phys.* **104**, 817–879 (2001).
468 50. Crutchfield, J. P. The calculi of emergence: computation, dynamics and induction. *Phys.*
469 *D Nonlinear Phenom.* **75**, 11–54 (1994).
470 51. Hopcroft, J. E., Motwani, R. & Ullman, J. D. *Introduction to Automata Theory,*
471 *Languages, and Computation*. (Pearson Education, 2008).
472 52. Moore, T. Y., Cooper, K. L., Biewener, A. A. & Vasudevan, R. Unpredictability of escape
473 trajectory explains predator evasion ability and microhabitat preference of desert rodents.
474 doi:10.1038/s41467-017-00373-2
475 53. Goldstein, R. E. Green Algae as Model Organisms for Biological Fluid Dynamics. *Annu.*
476 *Rev. Fluid Mech.* **47**, 343–375 (2015).
477 54. Simon, M. & Plattner, H. Unicellular Eukaryotes as Models in Cell and Molecular
478 Biology: Critical Appraisal of Their Past and Future Value. in *International Review of*
479 *Cell and Molecular Biology* **309**, 141–198 (Elsevier Inc., 2014).
480 55. Durham, W. M. *et al.* Turbulence drives microscale patches of motile phytoplankton. *Nat.*

481 *Commun.* **4**, (2013).

482 56. Mogilner, A. & Oster, G. Cell motility driven by actin polymerization. *Biophys. J.* **71**,
483 3030–3045 (1996).

484 57. Collins, J. J. & Stewart, I. N. Coupled nonlinear oscillators and the symmetries of animal
485 gaits. *J. Nonlinear Sci.* **3**, 349–392 (1993).

486 58. McNeill Alexander, R. *Principles of Animal Locomotion*. (Princeton University Press,
487 2003).

488 59. Wan, K. Y. & Jékely, G. On the unity and diversity of cilia. *Philos. Trans. R. Soc. Lond.*
489 *B. Biol. Sci.* **375**, 20190148 (2020).

490 60. Ahamed, T., Costa, A. C. & Stephens, G. J. Capturing the Continuous Complexity of
491 Behavior in C. elegans. doi:10.1101/827535

492 61. Stephens, G. J., Johnson-Kerner, B., Bialek, W. & Ryu, W. S. Dimensionality and
493 Dynamics in the Behavior of C. elegans. *PLoS Comput. Biol.* **4**, e1000028 (2008).

494 62. Berman, G. J., Choi, D. M., Bialek, W. & Shaevitz, J. W. Mapping the stereotyped
495 behaviour of freely moving fruit flies. *J. R. Soc. Interface* **11**, 20140672 (2014).

496 63. Stephens, G. J., Osborne, L. C. & Bialek, W. Searching for simplicity: Approaches to the
497 analysis of neurons and behavior. *Proc. Natl. Acad. Sci. U. S. A.* **108**, 15565–15571
498 (2010).

499 64. Kanagal, B. & Sindhwani, V. Rank Selection in Low-rank Matrix Approximations: A
500 Study of Cross-Validation for NMFs. in *Advances in Neural Information Processing*
501 *Systems* **23**, (2010).

502 65. Owen, A. B. & Perry, P. O. Bi-Cross-Validation of the SVD and the Nonnegative Matrix
503 Factorization. *Source Ann. Appl. Stat.* **3**, 564–594 (2009).

66. Ester, M., Kriegel, H.-P., Sander, J. & Xu, X. *A Density-Based Algorithm for Discovering Clusters in Large Spatial Databases with Noise*. (1996).

67. Kauffman, L. & Rousseeuw, P. J. *Finding Groups in Data: and introduction to cluster analysis*. (John Wiley & Sons, Inc., 1990). doi:10.1002/9780470316801

68. Kirkegaard, J. B., Marron, A. O. & Goldstein, R. E. Motility of Colonial Choanoflagellates and the Statistics of Aggregate Random Walkers. *Phys. Rev. Lett.* **116**, 038102 (2016).

69. M Cartmill. Climbing. in *Functional Vertebrate Morphology* 73–88 (Harvard University Press, 1985).

70. Markov, A. A. Extension of the Limit Theorems of Probability Theory to a Sum of Variables Connected in a Chain. *Notes Imp. Acad. Sci. St. Petersbg. VIII Ser. Physio-Mathematical Coll.* **22**, (1907).

71. Howard, R. A. *Dynamic and Probabilistic Systems, Volume 1: Markov models*. (Dover Publications, 1971).

72. Gagniuc, P. *Markov Chains: From Theory to Implementation and Experimentation*. (Wiley, 2017).

73. Billingsley, P. *Statistical Methods in Markov Chains*. *The Annals of Mathematical Statistics* **32**, 12–40 (Institute of Mathematical Statistics, 1961).

74. Crutchfield, J. P. & Young, K. Computation at the Onset of Chaos. in *Complexity, Entropy, and Physics of Information* (ed. Zurek, W.) (Addison-Wesley, 1989).

75. Crutchfield, J. P. & Young, K. Inferring statistical complexity. *Phys. Rev. Lett.* **63**, 105–108 (1989).

76. Moore, C. Dynamical recognizers: Real-time language recognition by analog computers.

527 *Theor. Comput. Sci.* (1998). doi:10.1016/S0304-3975(97)00028-5

528 77. Taylor, C. V. Demonstration of the function of the neuromotor apparatus in Euplotes by
529 the method of microdissection. *Naturwissenschaften* **9**, 910 (1921).

530 78. Okajima, A. & Kinosita, H. Ciliary activity and coordination in Euplotes eurystomus-I.
531 Effect of microdissection of neuromotor fibres. *Comp. Biochem. Physiol.* **19**, 115–131
532 (1966).

533 79. Bar-Ziv, R., Tlusty, T. & Libchaber, A. Protein-DNA computation by stochastic assembly
534 cascade. *Proc. Natl. Acad. Sci. U. S. A.* **99**, 11589–11592 (2002).

535 80. Guasto, J. S., Rusconi, R. & Stocker, R. Fluid Mechanics of Planktonic Microorganisms.
536 *Annu. Rev. Fluid Mech.* **44**, 373–400 (2012).

537 81. Goldstein, R. E., Polin, M. & Tuval, I. Noise and Synchronization in Pairs of Beating
538 Eukaryotic Flagella. *Phys. Rev. Lett.* **103**, 168103 (2009).

539 82. Párducz, B. Ciliary Movement and Coordination in Ciliates. *Int. Rev. Cytol.* **21**, 91–128
540 (1967).

541 83. Funfak, A. *et al.* Paramecium swimming and ciliary beating patterns: A study on four
542 RNA interference mutations. *Integr. Biol. (United Kingdom)* **7**, 90–100 (2015).

543 84. Kirkegaard, J. B., Bouillant, A., Marron, A. O., Leptos, K. C. & Goldstein, R. E.
544 Aerotaxis in the closest relatives of animals. *Elife* **5**, e18109 (2016).

545 85. Miño, G. L., Koehl, M. A. R., King, N. & Stocker, R. Finding patches in a heterogeneous
546 aquatic environment: pH-taxis by the dispersal stage of choanoflagellates. *Limnol.*
547 *Oceanogr. Lett.* **2**, 37–46 (2017).

548 86. Polin, M., Tuval, I., Drescher, K., Gollub, J. P. & Goldstein, R. E. Chlamydomonas
549 Swims with Two 'Gears' in a Eukaryotic Version of Run-and-Tumble Locomotion.

Science (80-.). **325**, 487–490 (2009).

87. Keeling, P. J. Combining morphology, behaviour and genomics to understand the evolution and ecology of microbial eukaryotes. *Philos. Trans. R. Soc. B Biol. Sci.* **374**, (2019).

88. Kahl, A. *Urtiere oder Protozoa.* (Fischer, 1935).

89. Yocom, H. B. The neuromotor apparatus of Euplotes patella. (University of California, Berkeley, 1917).

90. Kawamoto, T. & Kabashima, Y. Cross-validation estimate of the number of clusters in a network. *Sci. Rep.* **7**, 1–17 (2017).

561 **Figures**

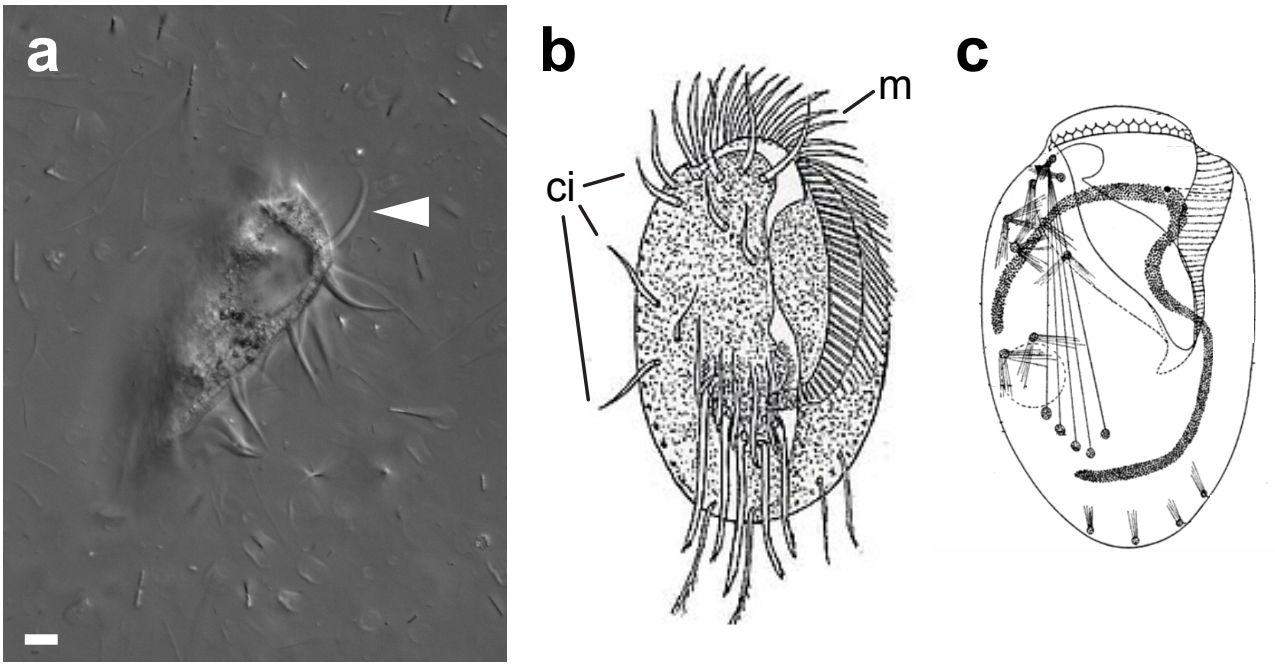

562

563 **Figure 1.** *Euplotes* exhibits highly polarized, complex cellular architecture and walks
564 across surfaces using microtubule-based organelles called cirri, some of which are physically
565 linked. Scale bar is 10 µm. **a**, A single *Euplotes eurystomus* cell in profile displays its ventral
566 cirri, which are used for walking locomotion across surfaces (arrowhead indicates a single cirrus
567 stretching out from the cell). **b**, A drawing of a *Euplotes* cell, viewed from the ventral surface,
568 highlighting the complex, asymmetric structure of the cell. Notable features include the cirri (ci)
569 and the membranellar band (m), wrapping from the top of the cell to the center, which is used to
570 generate a feeding current to draw in prey items. Drawing adapted and obtained from Wikimedia
571 Commons, from original source [88]. **c**, A drawing of a *Euplotes* cell, highlighting the fiber system
572 associated with the cirri, historically referred to as the neuromotor apparatus. Drawing adapted
573 from [89].

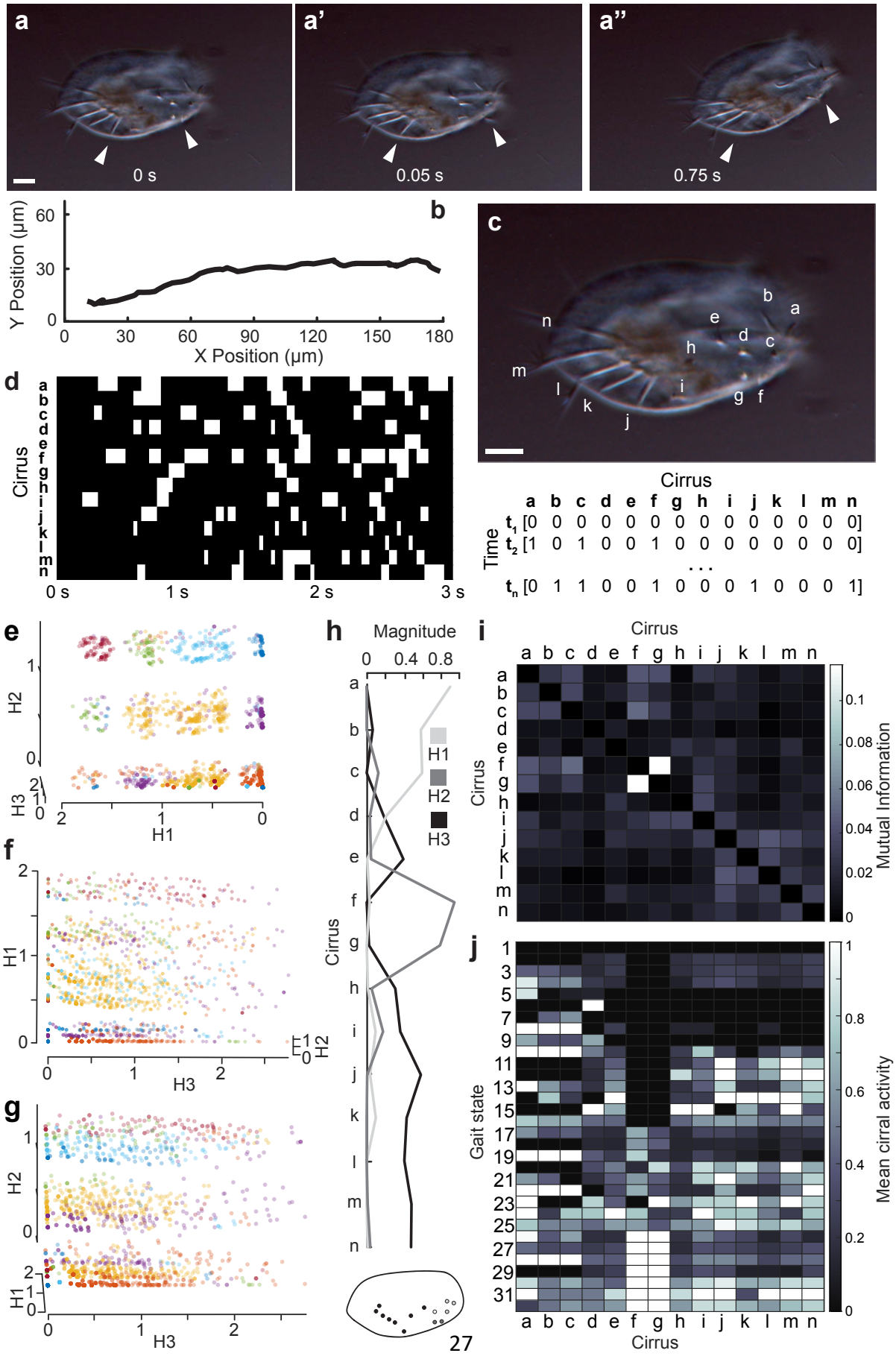
a
a'
a''
0 s
0.05 s
0.75 s
b
Y Position (μm)
X Position (μm)
c
d
Cirrus
0 s
1 s
2 s
3 s
Cirrus
Time
e
H2
H1
H3
f
H1
H3
H2
g
H2
H3
H1
h
Magnitude
Cirrus
H1
H2
H3
i
Cirrus
Mutual Information
j
Gait state
Mean cirral activity
Cirrus

575 **Figure 2.** The gait of *Euplotes* can be described in a discrete, reduced state space with gait
576 states corresponding to identifiable patterns of cirral activity. **a-a''**, The movements of cirri
577 during walking locomotion are clearly visible by brightfield microscopy by focusing on a plane
578 at the surface of the coverslip on which cells are walking. Three snapshots depict different time
579 points during a single walking trajectory, and white arrowheads indicate cirri. In the panels from
580 left to right, the cirrus indicated by the arrowhead on the left is stationary, stationary, and then
581 moving, and the cirrus indicated by the arrowhead on the right is stationary, moving, and then
582 stationary. Scale bar is 15 µm. **b**, The trajectory of a cell during a single recorded trajectory as
583 the cell walked across a coverslip from left to right. The cell position was manually tracked in
584 each frame. **c**, The scheme for encoding cirral dynamics during walking involved labeling each
585 of the 14 distinguishable ventral cirri (a-n), and recording cirral activity in each frame,
586 corresponding to timepoints (t_1,...,t_n), of recordings of walking cells as a 14-bit binary vector.
587 Each entry in each vector is given a value of either 0 if the cirrus is not moving and in contact
588 with the coverslip or 1 if the cirrus is moving. Scale bar is 15 µm. **d**, Representative visualization
589 of cirral dynamics for a single trajectory of a walking cell. These dynamics correspond to the
590 walking trajectory in **b**. Each row corresponds to a cirrus and each column is a single video
591 frame. White denotes cirral activity, a value of 1, in the vector encoding of dynamics from **c**.
592 Note the dynamical complexity and discrete, stepping-like nature of cirral movements. **e-**g,
593 Three roughly orthogonal views of a plot displays the structure of all recorded cirral dynamics
594 encoded as in Figure 2C from 13 cells over 2343 timepoints in a reduced state space obtained by
595 non-negative matrix factorization (NMF). Axes correspond to the components of the NMF (H1,
596 H2, H3), and each point is a single timepoint. Randomized colors highlight the 32 clusters
597 identified using the density-based spatial clustering of applications with noise (DBSCAN)

algorithm [66]. We refer to these clusters as gait states, and they correspond to unique configurations of cirral activity during walking locomotion (see panel F). **h**, Plot of the magnitudes associated with each cirrus corresponding to the components of the NMF of cirral dynamics shows distinct contributions from spatially distinct groups of cirri. Component H1, for example, is associated with activity in cirri a, b, and c. The tracing of a cell including the position of cirri has the same color map as the plot above and shows the grouping of the cirri corresponding to each component. **i**, A heatmap of mutual information between all pairs of cirri shows that correlations in cirral activity correspond to the NMF components displayed in **d**. For example, cirri a, b, and c share mutual information with one another and are the cirri contributing to component H1. **j**, A heatmap representation of the cirral activity associated with each of the 32 gait states. Values for each cirrus are the mean over all instances of the gait state. Note that each gait state has a unique signature of cirral activity.

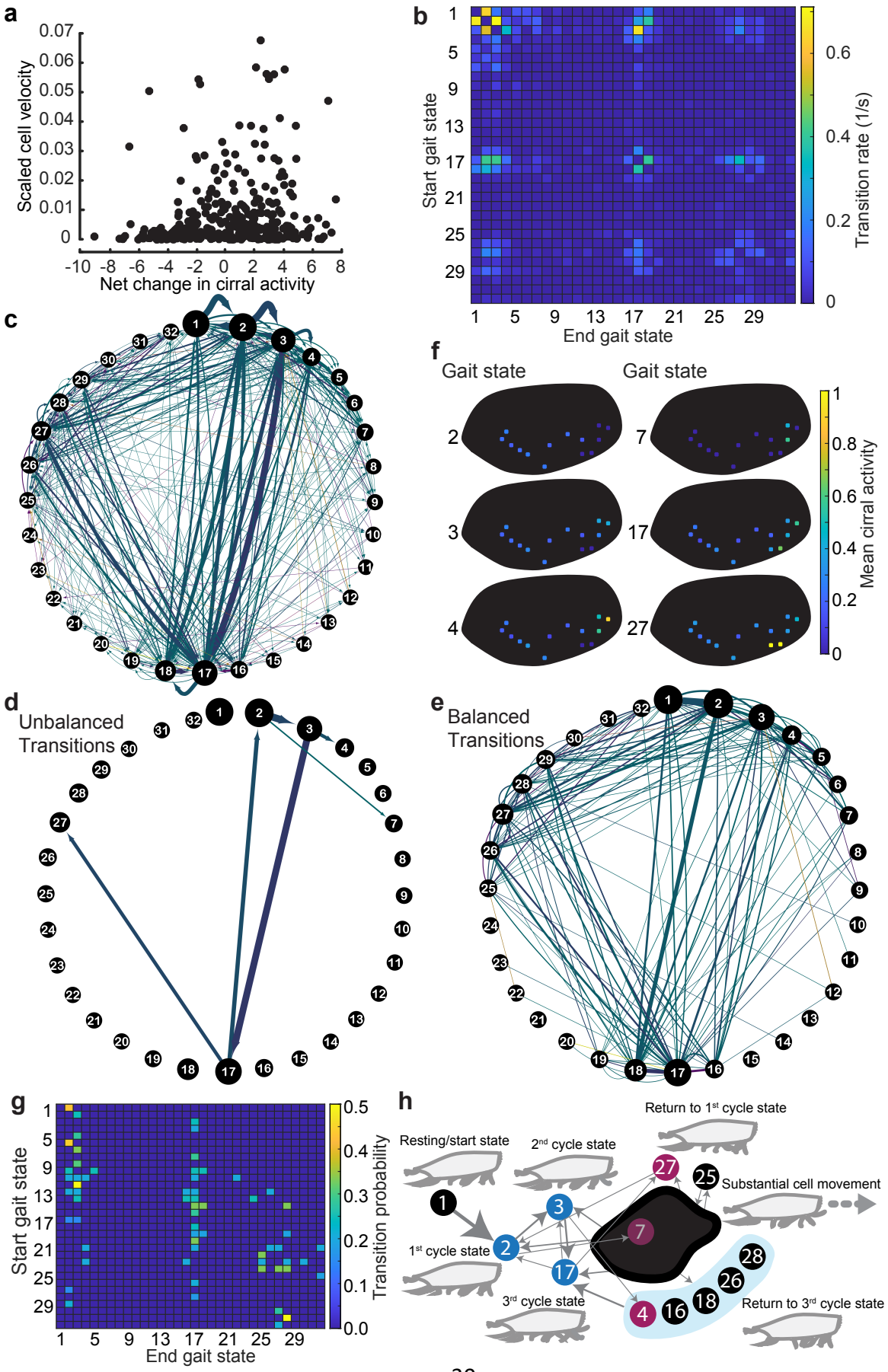
a
Scaled cell velocity
Net change in cirral activity
b
Start gait state
End gait state
Transition rate (1/s)
c
d
Unbalanced Transitions
e
Balanced Transitions
f
Gait state
Gait state
Mean cirral activity
g
Start gait state
End gait state
Transition probability
h
Resting/start state
2nd cycle state
Return to 1st cycle state
Substantial cell movement
1st cycle state
3rd cycle state
Return to 3rd cycle state

611

612 **Figure 3.** *Euplotes* walks with a cyclic stochastic gait exhibiting broken detailed balance,
613 stereotypy, and state machine-like dynamics. All data is pooled from the walking trajectories of
614 13 different cells over 2343 timepoints and 1423 pairwise gait state transitions. **a**, A plot of the
615 mean net change in cirral activity versus the net scaled cell velocity associated with all
616 transitions between the 32 gait states identified in Fig. 3 shows that the change in number of
617 active cirri is not strongly correlated with cell velocity (R^2=0.03). Cell velocities were obtained
618 from manually tracked walking trajectories and then scaled by dividing frame to frame
619 displacements for each trajectory by the length of the cell being tracked and also dividing by the
620 average frequency of cirral inactivity. Scaling provided a non-dimensional velocity scaled by
621 natural units of the system. Note that at low Reynolds number, velocity should be proportional to
622 force [44], so this plot also reflects the net walking force generated by the cell. Net change in cirral
623 activity was computed using the data presented in Fig. 3F. Note that the largest velocities are
624 associated with small negative and small to moderate positive net changes in cirral activity. **b**,
625 The transition matrix of all gait state transitions, with rows representing the starting state and
626 columns indicating the ending state, exhibits broken detailed balance. Rates were estimated by
627 dividing the total number of observed transitions between each state pair and dividing by the
628 total time observed. Under detailed balance or equilibrium conditions, transitions from one state
629 to another should be balanced by reverse transitions. Lack of this kind of reversibility, as seen by
630 the lack of symmetry of the heatmap across the diagonal, indicates broken detailed balance and
631 non-equilibrium dynamics. **c**, A directed graph representation of all gait state transitions. Nodes
632 correspond to the 32 gait states, and node sizes are scaled by the proportion of total time cells
633 spent in each state. Directed edges are represented by arrows between nodes and signify state
634 transitions. The size of the arrows is scaled by transition rates as in **b**. Edge color represents

635 scaled cell velocity as in **a**, with cool colors (more cyan) representing lower velocity, and
636 warmer colors (more magenta) representing higher velocity. **d**, A subset of transitions visualized
637 as in **c** shows the restricted and relatively high frequency nature of unbalanced, non-equilibrium-
638 like transitions. Only transitions that were observed to happen more than one time and exhibiting
639 a significant difference between forward and reverse transitions ($p<0.05$ by binomial test, see
640 Methods for more details) are displayed. **e**, A subset of transitions, similarly to panel E, except
641 that only the balanced transitions, lacking a significant difference between forward and reverse
642 transitions ($p<0.05$ by binomial test) are displayed, also show a complex and widespread
643 structure, this time of balanced, equilibrium transitions. Note that the majority of transitions
644 associated with high cell velocity involve equilibrium-like dynamics. **f,** Examples illustrating the
645 spatial organization of cirral activity corresponding to gait states. Some states, such as 7,
646 correspond to activity in spatially discrete groups of cirri, while others, such as 17, correspond to
647 cirral activity across the cell. The gait states displayed here are those involved in unbalanced
648 transitions. **g**, A heatmap of transition probabilities between states, showing only the most
649 probable transitions from a given state with all others set to zero, shows distinct structure. In
650 cases were multiple state transitions from a state were tied for the highest probability, all of these
651 transitions are displayed. Fewer than half of the total states are recipients of multiple high
652 probability transitions, and many states are the recipients of no high probability transitions. **h**, A
653 representation of functional states and transitions between them highlights the machine-like
654 nature of the gait of *Euplotes*. Gait states are represented as circles with numerical labels. Blue
655 circles represent states that are both recipients and sources of unbalanced transitions as identified
656 in **d** and constitute the three cycle states. Red circles represent states that are recipients but not
657 sources of unbalanced transitions as identified in **d**. Black circles correspond to gait states that

658 are associated only with balanced transitions as in **e**. States receiving no more than one unique
659 high probability transitions from states with only a single highest as identified in **g** were grouped
660 together into a compound state represented by the dark gray blob. The blue background behind
661 states 4, 16, 18, 26, and 28 indicates that these states all share the same highest probability
662 transitions between states identified in this panel, and thus, the group constitutes a single
663 compound functional state. Arrows represent the highest probability transitions between the
664 states, including compound states composed of multiple gait states as identified in Fig. 2 and 3
665 (dark gray blob and blue background). Gait state 1 is also depicted, as it is the state in which
666 cells spent the most time over all walking trajectories and also is uniquely the state from which
667 cells begin walking. Cells also frequently return to the state during walking. Further, transitions
668 from gait state 2 from gait state 1 constitute the single highest frequency transition. Together, all
669 identified states in this panel constitute functional states. Arrows represent the most probable
670 transitions between functional states, and all unbalanced transitions are also represented with size
671 scaled by their proportional probability compared to all other transitions emanating from the
672 source functional state. Cartoons are a walking cell in profile with cirri in a configuration
673 representative of the corresponding functional state. Labels refer to the apparent functional role
674 of states and their associated transitions. Beginning from gait state 1, the resting/start state, cells
675 are most likely to follow transitions from gait state 2 to 3 to 17 at which point cells are likely to
676 enter the functional state associated with substantial cell movement involving variable balanced
677 transitions between a number of gait states. Transitions are then likely to lead back toward the
678 cycle states. Note that while this representation of gait dynamics highlights the most probable
679 transitions, substantial variability, primarily involving reversible transitions, occurs during
680 walking trajectories.

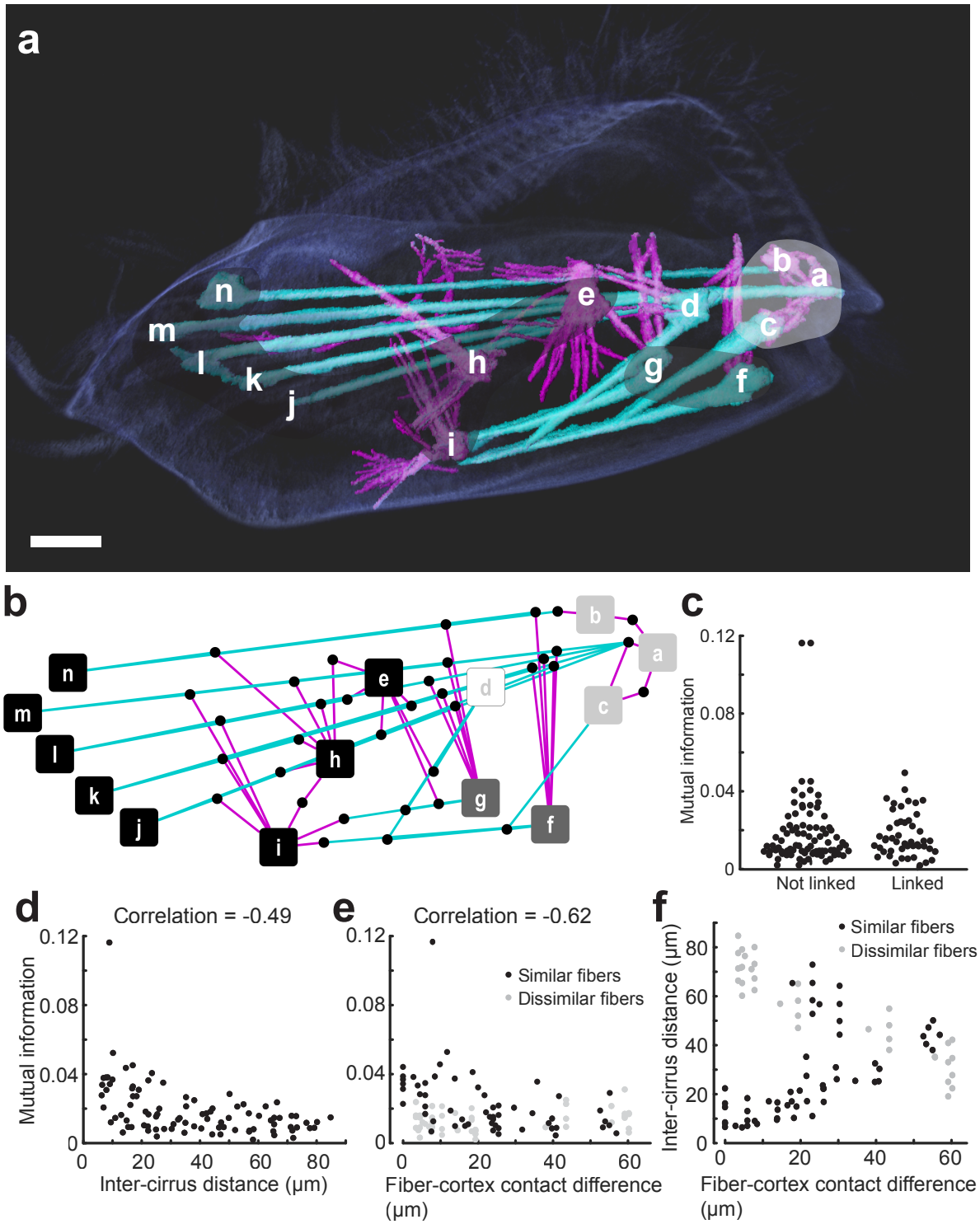

Figure 4. The fiber system of *Euplotes* is complex, interconnected, and constrains mechanistic hypotheses of gait coordination. **a**, The SiR-tubulin labeled cell (faint, dark blue) was imaged by confocal microscopy, and a 3D reconstruction as obtained from serial confocal

685 slices. Fibers were manually traced in each slice using TrakEM2 in FIJI. Two morphologically
686 distinct classes of fibers were observed and are indicated as follows: thick, linear fibers are cyan
687 and thinner, filamentous fibers are magenta (see Fig. S6 for raw image data). Fibers emanate
688 from the base of each cirrus and form a connected network between all cirri. The base of each
689 cirrus is indicated by corresponding letters (as in Fig. 2c). Gray shading indicates the dynamical
690 groups identified by dimensionality reduction and follows the same color scheme as in Fig. 3d.
691 Scale bar is 10 μm. **b**, A graph representation of fiber-fiber connections illustrates the complex
692 and interconnected nature of cirrus associated fiber topology. Nodes correspond to the cirri to
693 which each fiber system is associated, and edges indicate connections between fiber systems.
694 Colors of nodes indicate the same groups as in **a**, and colors of edges indicate the types of fibers
695 connecting to one another, cyan for thick fiber connections, magenta for thin fiber connections,
696 and purple for thick to thin fiber connections. **c**, Pairs of cirri that are linked by fiber-fiber
697 contacts show no statistically significant difference in mutual information compared to those
698 lacking fiber-fiber contacts. The plot displays mutual information between all pairs of cirri
699 grouped by the absence (Not linked) or presence (Linked) of associated fiber-fiber connections.
700 Statistical significance was evaluated by the Wilcoxon rank sum test. Note that when pairs of
701 cirri are grouped by fiber-fiber connection type, we do observe an increase in mutual information
702 for cirri associated with only thin fiber-fiber connection and only thick fiber-fiber connections
703 compared to those lacking fiber-fiber connections (see Fig. S6). **d**, A plot of mutual information
704 as a function of inter-cirrus distance displays negative correlation, with a Spearman correlation
705 coefficient of -0.49 ($p<0.001$). Plotted values are defined with respect to pairs of cirri. **e**, A plot
706 of mutual information as a function of fiber-cortex contact distance grouped by fiber type
707 similarity and lack thereof displays negative correlation, with a Spearman correlation coefficient

of -0.62 ($p<0.001$) for pairs of cirri with similar fiber types and no significant correlation for those with dissimilar fiber types. Similarity of fiber types is defined in terms of sharing at least some fiber types as defined in **a**. Fiber-cortex contact difference is measured by the mean cross nearest neighbor distance (see Methods) for all fiber-cortex contact points associated with each cirrus. The negative correlation values from the data plotted in **d** and **e** indicate that cirri that are closer to one another and also cirri with fiber-cortex contacts in nearby regions of the cell tend to have higher mutual information, and indeed cirri that are both close to one another and with similar patterns of fiber-cortex contacts display the highest mutual information. **f**, A plot of fiber-cortex contact difference versus inter-cirrus difference (as in panels **d** and **e**) illustrates that nearby cirri tend to have similar associated fiber-cortex contacts, highlighting that nearby cirri with similar fiber-cortex contacts share the most mutual information.

720 **Methods**

721 ***Cell husbandry***

722 Cultures of *Euplotes eurystomus* were obtained from Carolina Biological Supply Company (Item
723 #131480). Individual cells were isolated from cultures, which contained other protists and
724 meiofauna, by pipetting and placed in non-treated 6-well plates (Thermo Fischer Scientific 08-
725 772-49) containing spring water taken from cultures. Cells were kept in wells for no longer than
726 five days before imaging, and if cells were to be kept for longer than 48 hours, wells containing
727 cells were supplemented with 1% Cereal Grass Medium [1] (from Thermo Fischer Scientific
728 S25242) to prevent depletion of a population of prey bacteria and otherwise maintain *Euplotes*
729 under constant growth conditions.

730

731 ***Live cell brightfield microscopy***

732 Cells were concentrated by centrifugation (500×g for 5 min) and resuspended either in 0.5 mL of
733 spring water in coverglass bottomed FluoroDishes (World Precision Instruments FD35-100) or
734 in 0.2 mL spring water on a coverslip (FisherScientific, 12-545-D) for imaging. No more than
735 three cells were kept in 0.5 mL imaging samples and only one cell was ever kept in 0.2 mL
736 imaging samples in order to minimize cell-cell interactions. Cells were observed to exhibit
737 spontaneous walking activity on coverglass. Walking cells in FluoroDishes were imaged under
738 brightfield illumination using a Zeiss Z.1 Observer and Hamamatsu Orca Flash 4.0 V2 CMOS
739 camera (C11440-22CU) with a 20x, 0.8 NA Plan-Apochromat (Zeiss) objective. Cells on
740 coverslips were imaged under brightfield illumination with coverslips inverted over a well
741 containing a small amount of distilled water to reduce evaporation using a Zeiss Axio Zoom.V16
742 and a PCO pco.dimax S1 camera. Importantly, in both imaging systems, the focal plane was set

743 at the interface between cirri of walking cells and the glass surface upon which they were
744 walking. Images were acquired at 0.033 seconds per frame with a 0.005 second exposure in order
745 to capture all cirral dynamics during walking with minimal blur.
746
747 ***Quantification of walking dynamics***
748 Movies of walking cells were viewed using FIJI [2]. Movement of cirri, or lack thereof was
749 clearly visible in each movie frame (see Fig. 2a and Movie S1). The dynamical state of each
750 cirrus in each movie frame was manually annotated. For each frame, each cirrus received a label
751 of "1" if the cirrus was in motion and "0" if the cirrus was not moving and in contact with the
752 coverslip. Motion of cirri was evident in terms of a change in cirrus shape or tip position often in
753 addition to blur due to motion during image acquisition or position out of the focal plane (see
754 Fig. 2a and Movie S1). While only slowly walking cells were recorded, sometimes cells
755 nevertheless exhibit brief, spontaneous departures from slow walking during the course of movie
756 acquisition. Any frame in which the movement of the cell and/or cirri were too fast to be
757 resolved, such as during spontaneous escape responses[3] (Movie S2), was excluded from analysis
758 such that some videos were split into a number of separate continuous sequences. Thus, each
759 movie frame associated with a particular time point in the walking trajectory, with the exception
760 of those excluded from analysis as described, yielded a corresponding 14-element binary vector
761 encoding the motility state of the cell in terms of the movement of cirri. Cell movement was
762 tracked using the manual tracking feature of the TrackMate plugin in FIJI [4]. The center of each
763 cell was used as the reference feature for tracking. We analyzed the walking dynamics of 13
764 different cells.
765

766 ***Dimensionality reduction***

767 Dimensionality reduction was performed by non-negative matrix factorization (NMF)
768 implemented in MATLAB release 2019b (Mathworks, Natick). NMF was chosen as a
769 dimensionality reduction technique to allow us to obtain a reduced, sparse, and interpretable
770 representation of walking dynamics. Because NMF derives non-negative factors, the basis
771 vectors in NMF space correspond to patterns of cirral activity. NMF involves factoring data, A,
772 an n by m matrix, into non-negative factors W, an n by k matrix, and H, a k by m matrix where
773 the product $W*H$ approximates A. To determine the appropriate number of dimensions or rank, k,
774 that are necessary to accurately represent the data without overfitting, we performed cross-
775 validation by imputation with random holdouts [5,6], also implemented in MATLAB. We randomly
776 held out 15% of our walking dynamics data, performed NMF for a given k, and then used the
777 NMF reconstruction $W*H$, to update the missing data entries. This process of updating is known
778 as imputation, and we repeated the imputation process 50 times, by which point the imputed
779 values had stabilize, to obtain a final NMF reconstruction. We then computed the root mean
780 squared residual (RMSR) between the final NMF reconstruction, $W*H$, and our dataset, A. We
781 performed this entire process 100 times for each value of k. As is generally the case for NMF, we
782 observed a monotonic decrease in reconstruction error with increasing k without performing the
783 imputation procedure [7] (Fig. S2a). In contrast to this trend, we observed an increase in RMSR of
784 imputed values with increasing k indicating overfitting [5] (Fig. S2b). We chose k=3 because this
785 value was the highest value before a notable increase in imputation error (Fig. S2b), which
786 would indicate overfitting [5,6]. Thus, our choice of rank 3 selects the lowest rank approximation
787 that captures structure of the dataset without overfitting that structure. Further, our choice

788 facilitated the visual inspection of the structure of data in the reduced dimensional
789 reconstruction.
790 Finally, we noted that for our chosen value of *k*, due to the stochastic nature of the NMF
791 algorithm, which involves a random initialization step, we obtained slightly different solutions
792 for different iterations [5]. In order to choose the best reduced dimensional approximation,
793 therefore, we performed NMF 500 times and chose the particular solution corresponding to the
794 lowest RMSR compared to our dataset.
795
796 ***Clustering***
797 Clustering on the dataset obtained using NMF was performed by density-based spatial
798 clustering of applications with noise (DBSCAN) algorithm [8] implemented in MATLAB release
799 2019b (Mathworks, Natick). Structure in NMF space was clearly visible (Fig. 2e-g), and
800 DBSCAN using a Euclidean distance metric, was initially chosen as a clustering method because
801 it yielded qualitatively good partitioning of the data. The DBSCAN algorithm involves stochastic
802 search within neighborhoods of a given radius ε around datapoints, and points with a minimum
803 number of neighbors, *n*, within their neighborhood are grouped as belonging to the same cluster,
804 leaving two free parameters to determine. We set ε by first using the
805 clusterDBSCAN.estimateEpsilon function in MATLAB (release 2020b, Phased Array System
806 Toolbox), which yielded a value of 0.15. We next set about determining the minimum neighbor
807 number, *n*. To do so, we computed the average Silhouette coefficient, a commonly used measure
808 of clustering quality that indicates how well-separated clusters are [9], for various values of *n*. The
809 results of this analysis are plotted in Fig. S3. Higher Silhouette coefficients indicate better
810 clustering, and we found that a value of n=8 maximized the mean Silhouette coefficient (Fig.

S3a). We also noted, however, that for this value, many datapoints were found to be outliers, not belonging to any cluster due to having too few points within a distance of ε. Fig. S3b displays percentage of datapoints found to be outliers as a function of *n*. In order to avoid categorizing more than 5% of datapoints as outliers, we chose to settle on *n*=4, which does not have a significantly different mean Silhouette coefficient compared to any of the others in the range *n*=2-7. This choice was further supported by the fact that major clusters involving more than 5 datapoints identified with *n*=8 were also identified with *n*=4.

Although this set of parameters gave qualitatively and quantitatively reasonable clustering results, we sought to further refine our clusters and to further reduce the outlier datapoints. We noted the obvious partitioning of the NMF dataset into three groups along the H2 axis (Fig. 2e). We found the previously determined parameter values to yield good clustering for the top and middle partitions ($H2 \leq 1.1$ and $0.2 < H2 < 1.1$), with no outliers. For the lower partition ($H2 \leq 0.2$), however, we found that we were able to improve clustering by using ε=0.1182. With this updated value, we found no statistically significant change in Silhouette coefficient and reduced outliers to 0%. The clusters obtained by this process constituted the identification of the 32 gait states. We note here that the problem of determining the true or optimal number of clusters is an unresolved problem [10], and we note that we have followed standard methods to determine cluster number, and we found that our key results do not depend sensitively on the precise number of clusters identified (see following section and Fig. S8 for more details).

State transition analysis

Following dimensionality reduction and clustering to identify gait states, we proceeded to characterize state transition dynamics. For each cell trajectory, we identified all unique gait state

transitions for a total of 1423 unique pairwise transitions over the cumulative 2343 video frames for 77.14 s of recording. We computed empirical transition rates between states as the total number of observed transitions divided by the total time of observation. In order to determine which transitions were balanced and which were unbalanced, we followed Chang and Marshall [11], and performed binomial tests of statistical significance. Assuming a system at equilibrium, with all transitions obeying detailed balance, we expect to observe some deviation from exactly reciprocal transitions and can calculate the probability of observing a given set of ratios given underlying probabilities of forward and reverse transitions. The binomial probability of observing a set of transitions with known forward and reverse probabilities is given by

$$P(X = f) = \binom{n}{f} p_{forward}^{f} p_{reverse}^{n-f}$$

where $\binom{n}{f} = \frac{n!}{f!(n-f)!}$ is the choose function, f is the number of forward transitions, n is the total number of transitions (such that n-f is the number of reverse transitions), and the probabilities $p_{forward}$ and $p_{reverse}$ are the forward and reverse probabilities. Considering only the set of transitions involving a specific pair of states, and calculating the probability that a transition between those states is either in the forward or reverse direction, the values of forward and reverse probabilities in the balanced case must be equal such that $p_{forward} = p_{reverse} = 0.5$. With an α level of 0.05, we then considered reciprocal transition pairs with binomial probabilities less than 0.05 to be significantly unbalanced. Figure S9 displays the binomial probabilities associated with all transitions.

In order to calculate the estimated entropy production rate, we followed Wan and Goldstein [12], where the entropy production rate is defined as

$$\dot{S} = \frac{1}{2} \sum_{i \neq j} J_{ij} A_{ij}$$

856

857 with conjugate fluxes $J_{ij} = p_i k_{ij} - p_j k_{ji}$ and forces $A_{ij} = \ln\left(\frac{p_i k_{ij}}{p_j k_{ji}}\right)$ where the p_l are the

858 probabilities of being in state *l* at steady state and the k_{ij} are the transition rates between states *i*

859 and *j*. We estimate the state occupancy probabilities p_l as $\frac{T_l}{T_{Total}}$, where T_l is the amount of time

860 spent in state *l* over all trajectories and T_{Total} is the total recorded time, and the rates k_{ij} as $\frac{N_{ij}}{T_i}$,

861 where N_{ij} is the total number of observed transitions from state *i* to state *j* and T_i is the total time

862 spent in state *i*. To avoid $k_{ji} = 0$, we let $k_{ji} = \frac{1}{p_j T_{max}}$ where $T_{max} = 11.55$ seconds is the

863 maximum duration of any single recorded walking trajectory.

864 In the course of our state transition analysis, we also checked whether the waiting times

865 between instances of each state might be non-exponentially distributed, with exponential

866 distributions indicative of an embedded Markov process or possibly self-organized criticality

867 [13,14]. Using the Lilliefors test implemented in Matlab, we found that in general, waiting times

868 were not exponentially distributed, although states 2, 3, 6, 16, 17, 18, 25, 27, 28, 32 were found

869 to have waiting times consistent with exponential distributions with Benjamini-Hochburg

870 corrected p-values of 0.046, 0.046, 0.022, 0.008, 0.046, 0.017, 0.046, 0.0081, 0.0046, 0.0046

871 respectively. Interestingly, none of the waiting times between the movements of individual cirri

872 were found to be consistent with exponential distributions. These results are consistent with

873 mechanisms constraining the temporal dynamics of cirri and state transitions.

874 In order to begin evaluating whether state transitions obeyed the Markov property, where

875 the transition probabilities from one state to the next are completely determined by current state

876 [15,16], we estimated the transition matrix for walking dynamics, consisting of the transition

877 probabilities between all states. We estimate the transition probability from state *i* to state *j* as

878 $p_{ij} = \frac{N_{ij}}{\sum_k N_{ik}}$ such that $\sum_i p_{ij} = 1$. The entries of the transition matrix, P, are these transition

879 probabilities with indices i for rows and j for columns. If gait state transitions obeyed the Markov

880 property, we expect that the product of the transition matrix with itself, P^2, would be equivalent

881 to the two-step transition matrix where transition probabilities are computed as before except that

882 state j is the state to which i has transitioned after an intervening transition. Figure S5 displays

883 the results of this analysis showing that the two matrices show substantial quantitative and

884 qualitative differences. Although these results strongly suggest violation of the Markov property,

885 we applied the Billingsley test for a more statistically rigorous evaluation [17,18]. This test was

886 implemented and performed in Matlab (release 2019b). The Billingsley test gives a χ^2 metric

887 with M^2-2M degrees of freedom given by

888 $$\sum_{i=1}^{M} \sum_{j=1}^{M} \frac{\left(N_{ij} - R_{ij} \sum_{j=1}^{M} N_{ij}\right)^2}{R_{ij} \sum_{j=1}^{M} N_{ij}},$$

889 where R_{ij}, the independent trials probability matrix, is given by

890 $$R_{ij} = \sum_{k=1}^{M} N_{kj} / \left(\sum_{h=1}^{M} \sum_{l=1}^{M} N_{hl} - \sum_{k=1}^{M} N_{ik}\right).$$

891 Importantly, we also noted that the key qualitative results of our state transition analysis

892 are robust to the details of clustering results. In particular, we find that strongly unbalanced

893 transitions and violation of the Markov property exist for a range of clustering parameters.

894 Figure S8 displays the transition matrices for different clustering results.

895

896 ***Confocal microscopy***

897 Cells were prepared for imaging and placed into a FluoroDish as described in the Live Cell

898 Brightfield Microscopy section. Cells were then labeled with SiR-tubulin (Spirochrome provided

899 by Cytoskeleton, Inc, CY-SC002) at 1 μM concentration. Cells were imaged using a Zeiss LSM

900 880 AxioExaminer and a 40x, 1.2 NA C-Apochromat water immersion objective (Zeiss) and
901 excitation provided by a 633 nm laser (Zeiss). Only one full confocal z-stack of a complete cell
902 was obtained during imaging to avoid effects of photodamage.
903
904 ***Fiber reconstruction and analysis***
905 The image stack resulting from confocal imaging was first aligned in FIJI using the
906 StackReg plugin [2]. Next, fibers were manually segmented in each of the aligned z-stack images
907 using the TrakEM2 plugin in FIJI [19,20]. Thick and thin fibers (Fig. 5a) were morphologically
908 distinguished, with thick fibers having a diameter of no less than 5 µm at the thinnest point.
909 Fibers were traced from their distal termini to their convergences at the base of the cirri with
910 which they were associated. Following segmentation, 3D surfaces were reconstructed in
911 TrakEM2. Inter-fiber contacts were then found by inspection of 3D reconstructions and verified
912 by examining individual z-stack frames to confirm intersections between fibers.
913
914 **References**
915 1. King, N., Young, S. L., Abedin, M., Carr, M. & Leadbeater, B. S. C. Starting and
916 maintaining Monosiga brevicollis cultures. *Cold Spring Harb. Protoc.* **4**, (2009).
917 2. Schindelin, J. *et al.* Fiji: an open-source platform for biological-image analysis. *Nat.*
918 *Methods* **9**, 676–682 (2012).
919 3. Ricci, N., Giannetti, R. & Miceli, C. The ethogram of Euplotes crassus (ciliata,
920 hypotrichida): I. The wild type. *Eur. J. Protistol.* **23**, 129–140 (1988).
921 4. Tinevez, J. Y. *et al.* TrackMate: An open and extensible platform for single-particle
922 tracking. *Methods* **115**, 80–90 (2017).

5. Kanagal, B. & Sindhwani, V. Rank Selection in Low-rank Matrix Approximations: A Study of Cross-Validation for NMFs. in *Advances in Neural Information Processing Systems* **23**, (2010).

6. Owen, A. B. & Perry, P. O. Bi-Cross-Validation of the SVD and the Nonnegative Matrix Factorization. *Source Ann. Appl. Stat.* **3**, 564–594 (2009).

7. Wold, S. Cross-Validatory Estimation of the Number of Components in Factor and Principal Components Models. *Technometrics* **20**, 397–405 (1978).

8. Ester, M., Kriegel, H.-P., Sander, J. & Xu, X. *A Density-Based Algorithm for Discovering Clusters in Large Spatial Databases with Noise*. (1996).

9. Ronan, T., Qi, Z. & Naegle, K. M. Avoiding common pitfalls when clustering biological data. *Science Signaling* **9**, re6–re6 (2016).

10. Kawamoto, T. & Kabashima, Y. Cross-validation estimate of the number of clusters in a network. *Sci. Rep.* **7**, 1–17 (2017).

11. Chang, A. Y. & Marshall, W. F. Dynamics of living cells in a cytomorphological state space. *Proc. Natl. Acad. Sci. U. S. A.* **116**, 21556–21562 (2019).

12. Wan, K. Y. & Goldstein, R. E. Time Irreversibility and Criticality in the Motility of a Flagellate Microorganism. *Phys. Rev. Lett.* **121**, 58103 (2018).

13. Bak, P., Tang, C. & Wiesenfeld, K. Self-organized criticality: An explanation of the 1/f noise. *Phys. Rev. Lett.* **59**, 381–384 (1987).

14. Sánchez, R., Newman, D. E. & Carreras, B. A. Waiting-Time Statistics of Self-Organized-Criticality Systems. *Phys. Rev. Lett.* **88**, 4 (2002).

15. Markov, A. A. Extension of the Limit Theorems of Probability Theory to a Sum of Variables Connected in a Chain. *Notes Imp. Acad. Sci. St. Petersbg. VIII Ser. Physio-*

Mathematical Coll. **22**, (1907).

16. Gagniuc, P. *Markov Chains: From Theory to Implementation and Experimentation*. (Wiley, 2017).
17. Billingsley, P. *Statistical Methods in Markov Chains*. *The Annals of Mathematical Statistics* **32**, 12–40 (Institute of Mathematical Statistics, 1961).
18. Hiscott, R. N. *Chi-Square Tests for Markov Chain Analysis*. *Mathematical Geology* **13**, (1981).
19. Cardona, A. *et al.* TrakEM2 Software for Neural Circuit Reconstruction. *PLoS One* **7**, e38011 (2012).
20. Thévenaz, P., Ruttimann, U. E. & Unser, M. A pyramid approach to subpixel registration based on intensity. *IEEE Trans. Image Process.* **7**, 27–41 (1998).

Acknowledgements

We would like to thank the students and faculty of the 2016 Marine Biological Laboratory Physiology Course and current and former members of the Marshall Lab and King Lab for comments, critiques, and encouragement during the development of this project. We would also like to thank David Booth and Dennis Bray for comments on the manuscript. This work was supported in part by the I2CELL Seed Award of the Fourmentin-Guilbert Scientific Foundation (to WFM), NIH grant R35 GM130327 (to WFM), NSF grant MCB- 2012647 (to WFM), and the Merck Fellowship of the Jane Coffin Childs Memorial Fund for Medical Research (to BTL).

Author contributions

BTL, JDP, and WFM conceived of the study and developed analyses. BTL collected data. BTL, JG, JDP, and WFM interpreted the data. BTL and JG performed analyses. BTL and WFM wrote the paper.

Competing interests

The authors declare no competing interests.

Supplementary Information is available for this paper including Figures S1-S9 and Movies S1 and S2.